










Reversible metal-insulator transition in SrIrO₃ ultrathin layers by field effect control of inversion symmetry breaking

Fernando Gallego ^{1,2}, Javier Tornos¹, Juan Ignacio Beltran ¹, Andrea Peralta ¹, Javier Garcia-Barriocanal³, Guichuan Yu^{3,4}, Geoffrey Rojas³, Carmen Munuera^{2,5}, Mariona Cabero ^{6,7}, David Sanchez-Manzano ¹, Fabian Cuellar ¹, Gabriel Sanchez-Santolino ^{1,2}, Zouhair Sefrioui^{1,5}, Alberto Rivera-Calzada ^{1,5}, Federico Jose Mompean^{2,5}, Mar Garcia-Hernandez^{2,5}, Carlos Leon^{1,5}, Maria del Carmen Muñoz⁸ & Jacobo Santamaria ^{1,5}✉

SrIrO₃ is a correlated semimetal with narrow t_{2g} d-bands of strong mixed orbital character resulting from the interplay of the spin-orbit interaction due to heavy iridium atoms and the band folding induced by the lattice structure. In ultrathin layers, inversion symmetry breaking, occurring naturally due to the presence of the substrate, opens new orbital hopping channels, which in presence of spin-orbit interaction causes deep modifications in the electronic structure. Here, we show that in SrIrO₃ ultrathin films the effect of inversion symmetry breaking on the band structure can be externally manipulated in a field effect experiment. We further prove that the electric field toggles the system reversibly between a metallic and an insulating state with canted antiferromagnetism and an emergent anomalous Hall effect. This is achieved through the spin-orbit driven coupling of the electric field generated in an ionic liquid gate to the electronic structure, where the electric field controls the band structure rather than the usual band filling, thereby enabling electrical control of the effective role of electron correlations. The externally tunable antiferromagnetic insulator, rooted in the strong spin-orbit interaction of iridium, may inspire interesting applications in spintronics.

¹GFMC, Universidad Complutense de Madrid, 28040 Madrid, Spain. ²2D-Foundry Group, Instituto de Ciencia de Materiales de Madrid ICMM-CSIC, 28049 Madrid, Spain. ³Characterization Facility, University of Minnesota, 55455 Minneapolis, MN, USA. ⁴Informatics Institute, University of Minnesota, 55455 Minneapolis, MN, USA. ⁵Unidad Asociada UCM-ICMM CSIC “Laboratorio de Heteroestructuras con Aplicación en Spintrónica” Instituto de Ciencia de Materiales de Madrid ICMM-CSIC, 28049 Madrid, Spain. ⁶IMDEA Nanoscience Institute. Campus Universidad Autonoma, 28049 Madrid, Spain. ⁷Centro Nacional de Microscopia Electronica. Universidad Complutense, 28040 Madrid, Spain. ⁸Instituto de Ciencia de Materiales de Madrid ICMM-CSIC, 28049 Madrid, Spain. ✉email: jacsan@ucm.es

5d oxides have recently gathered a lot of attention due to the possibility of new electronic ground states resulting from the interplay between spin orbit and Coulomb interactions¹. The strong spin orbit interaction due to the large atomic number *5d* element splits the *d* bands allowing for the moderate Coulomb repulsion (*U*) to drive significant electron correlation effects². Strontium iridates of the Ruddlesen-Popper series Sr_{*n*+1}Ir_{*n*}O_{3*n*+1} are an interesting family of compounds where the first 214 member is a spin orbit Mott insulator^{3–8} with a Coulomb gap opening in the narrow $J_{\text{eff}} = 1/2$ band. Increasing the index *n* progressively narrows the gap and the end member $n = \infty$ is the perovskite 113 Sr iridate (SIO) which shows a paramagnetic semi-metallic ground state^{6–8}. It has been proposed that the reduced connectivity of the Ir sublattice by the rock salt SrO blocks in the unit cell of the first members of the series reduces the bandwidth (*W*) and effectively increases the relative strength of the Coulomb repulsion U/W ^{9,10}. While in the 113 its surprisingly narrow electron and hole bands crossing the Fermi level (responsible for the highly compensated semi-metallic state) underscore the coupling of the electronic structure to the IrO₆ octahedral rotations which causes backfolded bands and mixing of $J_{\text{eff}} = 1/2$ and $J_{\text{eff}} = 3/2$ states¹¹. This system is in the vicinity of a metal-to-insulator transition, what in view of the similar energy scales (0.3–0.4 eV) of Coulomb repulsion, band width (kinetic energy), and spin orbit interaction raises intriguing questions on the interplay between spin orbit and Mott physics. This is probably related to the metal to insulator (MIT) transition displayed by SIO thin films grown on SrTiO₃ (STO) when thickness is reduced down to the nanometer scale^{12,13}. First-principles calculations have shown concomitant anti-ferromagnetism developing at the transition^{12,13}. However, at the moment it is not clear whether the MIT transition is driven by enhanced correlations in two dimensions or by the emergent magnetic state at the transition. Fundamentally, establishing the origin of the MIT is a major question whose answer could signal the possibility of engineering a spin-orbit Mott insulator.

The controlled growth of transition metal oxides with strong spin orbit interaction down to the unit cell thickness, opens the possibility to study the interplay between quantum confinement, spin orbit interaction and electron correlations. Spin-orbit interaction couples electron spin to its motion in the electric field generated by the lattice potential. In crystal lattices with broken inversion symmetry as bulk wurtzite or zinc blende semiconductors, the spin orbit interaction lifts the Kramers degeneracy and splits electron bands^{14,15}. These effects are also present in 2D electron gases where the absence of inversion symmetry, naturally broken in the growth direction, creates an additional electric field¹⁶. In transition metal oxides ultrathin films, the multiorbital nature of *d* electrons together with the

possibility of choosing ions with large atomic number opens interesting new avenues for the interplay between spin orbit interaction and symmetry breaking^{17–19}. Spin orbit interaction mixes t_{2g} bands (corresponding to d_{xy} , d_{xz} , and d_{yz} orbitals) of different spin and orbital symmetry and yields narrow bands resulting from the spin orbit splitting where Coulomb interaction kicks in ref. ². Inversion symmetry breaking, on the other hand, opens new hopping channels and influence orbital mixing, band width and eventually also spin splitting^{17–20}. Moreover, the large electric fields generated in field effect experiments with ionic liquids can be used as an efficient knob to modulate symmetry-breaking fields (meant here in the sense of breaking of inversion symmetry of an ultrathin layer in the 2D limit by the presence of the substrate and further modulated by an applied electric field) and accordingly produce drastic changes in the electronic structure, strongly coupled to the electric field by the strong spin orbit interaction, allowing for the stabilization of novel correlated electronic states.

In this paper, we report ionic liquid gating^{21–27} of ultrathin SIO 113 layers in the vicinity of the MIT. Complexities related to the generation of oxygen vacancies and /or SIO degradation by the ionic liquid were carefully excluded (See Methods and Supplementary Note 1). The large electric field built up at the interface between the ionic liquid and the oxide due to the formation of the Electric Double Layer (EDL), is typically screened over the Thomas Fermi length. SIO 113 iridate is a bad metal due to a high degree of carrier (electron-hole) compensation and, as a result, its screening length becomes nanometric, closely matching the thickness range where SIO 113 thin films become insulating. The incomplete screening of the electric field by the small carrier density of SIO 113, which is further reduced at the MIT, is key for the observation of effects of the electric field beyond electrostatic doping. In particular, we will examine modulations of the electronic structure driven by its coupling to the electric field by the spin-orbit interaction^{17–20}. It is important to remark that this result is different to the modification shown before²⁸ of the Dzyaloshinskii-Moriya interaction (DMI) in the SrRuO₃ by the small electric field developing in STO back gating. In our case, the very strong electric field generated by the ionic liquid gate modulates the inversion asymmetry (already broken by the substrate) and couples to the electronic structure of the SrIrO₃ thin film through the strong spin orbit interaction triggering a MIT.

Results and discussion

Structural characterization. SIO 113 ultrathin films grown on (001) STO with thickness in the range 1–3 nm exhibited a metal-to-insulator transition below 2 nm as shown in Fig. 1. Specular X-ray diffraction experiments evidence an enlargement of the out

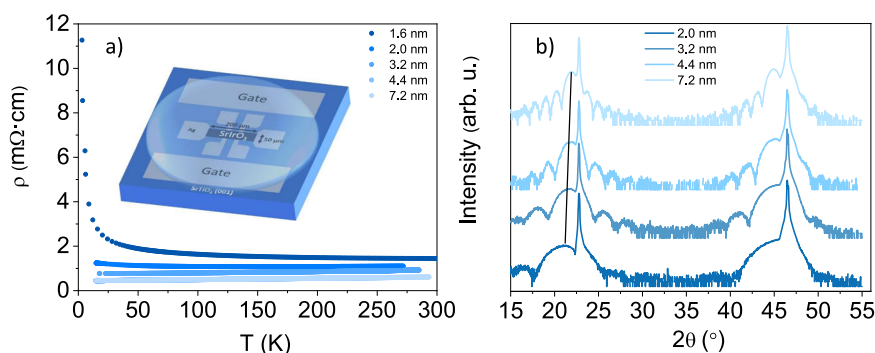


Fig. 1 Samples characterization as function of thickness. **a** Resistivity as a function of temperature of SrIrO₃ ultrathin films grown on SrTiO₃. **b** Specular x-ray diffraction of SrIrO₃ ultrathin films grown on SrTiO₃. Sketch of the contact lay-out for the ionic liquid gating experiment in the side gating geometry.

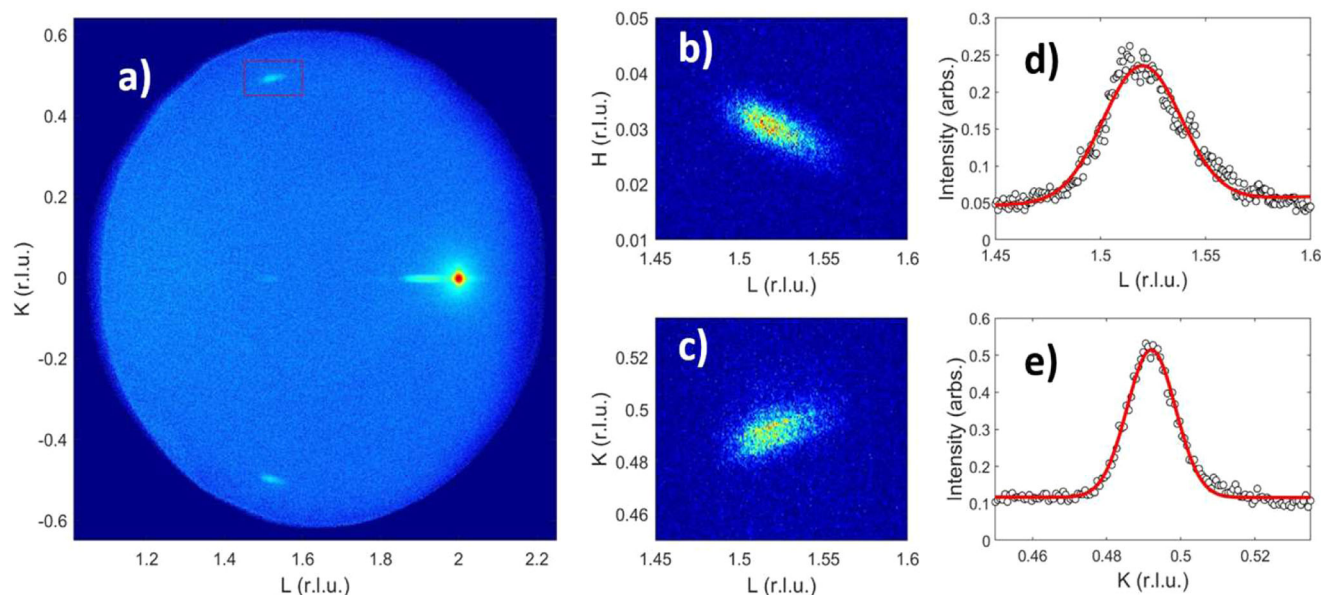


Fig. 2 Reciprocal space map characterization of a 5 nm SrIrO₃ thin film. **a** Reciprocal space map of a 5 nm SrIrO₃ ultrathin film grown on SrTiO₃ showing the X-ray diffraction reflections projected on the KL plane. The contour plot uses a logarithmic false color scale and it shows half-integer reflections (0, −0.5, 1.5), (0, 0.5, 1.5), and (0, 0, 1.5) corresponding to the pseudocubic unit cell of the iridate, as well as the integer (0 0 2) reflections of both film and substrate. **b, c** Linear false color scale contour plots of HL and KL projections of the (0, 0.5, 1.5) reflection highlighted with a red box in **a**. **d, e** Intensity profiles of the map displayed in **c** along the horizontal and vertical axis respectively.

of plane lattice parameter when the thickness is reduced, as inferred from a shift of diffraction peaks to lower angles when thickness is reduced (see inclined line in Fig. 1 connecting (002) diffraction peaks).

This indicates structural modifications concomitant with the thickness-controlled MIT transition. To explore the effect of oxygen rotations on the reduced symmetry of the unit cell we have conducted three-dimensional X-ray reciprocal space imaging. Figure 2 shows reciprocal space maps of the 5 nm sample with reflections indexed with (H , K , and L) triads referred to the cubic unit cell of the SrTiO₃ substrate. Non integer reflection both in in-plane and out of plane axes can be clearly recognized indicating the rotation of oxygen octahedra around both in plane and out of plane axes similar to the bulk SrIrO₃². The mixed $\{0, \pm K/2, L/2\}$, $\{\pm H/2, 0, L/2\}$ and $\{\pm H/2, \pm K/2, L/2\}$ reflections are thus an indication for a $a^-a^-c^+$ pattern of the oxygen octahedra^{29–31}. This pattern arises from the out-of-phase rotation of oxygen octahedra in the plane of the film layers combined with out of plane tilting and antipolar displacements of A site cations^{30,31}. This shows that the antiferrodistortive in plane rotations $a^0a^0c^-$ which have been shown to occur in the SIO at layer thickness below 1 nm¹³, relax into the 3D rotation pattern of the Pbnm space group of bulk samples when thickness is increased from one to four unit cells. This rotation pattern was consistently observed in a series of samples with thickness varied between 2 and 10 nm, a thickness range where the films are metallic.

Ionic liquid gating. Ionic liquid gating was performed in the side gating geometry (see sketch in Fig. 1). We selected samples at the verge of the MIT (Fig. 1a) in the insulating (1.6 nm) and metallic (2 nm) sides of the transition and carried out the ionic liquid gating experiments in these samples to cross the MIT from both sides (See Fig. 3). At each gate voltage simultaneous measurements of longitudinal resistivity (Fig. 3a, b) and Hall effect (Fig. 3c, d) were conducted. Ionic liquid gating turned the conducting state of the samples from

metal to insulating and vice versa. Interestingly, as discussed below, the effect of the gating was opposite to what is expected from electrostatic doping. The metallic 2 nm sample (left panels with data marked in red color in Fig. 3) turns into insulating when positive gate voltages are applied (expected to produce electron doping). Conversely, the insulating 1.6 nm sample (right panels with data marked in blue color in Fig. 3) turns into metallic under negative gate voltages (expected to produce hole doping).

Hall effect measured at 40 K for the different gate voltages were used to examine the changes in the carrier density resulting from the gating process. This temperature is high enough to avoid the effects of quantum corrections to the conductivity or to the magnetoresistance of magnetic phases which, as discussed below, emerge at low temperatures. Transverse resistivity had always a negative slope indicating larger mobility for electrons than for holes in agreement with previous reports^{11,31,32}. On the metallic side of the transition, for the 2 nm thick samples, when the sample is gated with positive voltages (expected to produce electron doping) an increase of the Hall resistivity is detected, which could in principle be understood in terms of a decrease of the hole density in a two-band picture. On the other hand, on the insulating side of the transition, when the sample is gated with negative voltages, the Hall resistivity decreases, which could be understood in terms of an increase of the hole density in a two-band picture. A rough quantitative analysis of the carrier density can be done following reference³². Assuming charge compensation and larger mobility for electrons than for holes (see Supplementary Note 2 and Supplementary Figures S3 and S4) the analysis yields, in the metallic state, values of the carrier densities for holes $n_h = 10^{20} \text{ cm}^{-3}$ and electrons $n_e = 7 \times 10^{19} \text{ cm}^{-3}$ with mobilities in the range 30–40 cm²/Vs being larger for electrons than for holes. These values are comparable to those reported in backgating experiments producing much weaker changes in the resistivity³². In the insulating state carrier densities dropped to $n_h = 2 \times 10^{19} \text{ cm}^{-3}$ and $n_e = 1 \times 10^{19} \text{ cm}^{-3}$ while mobility values were little affected by

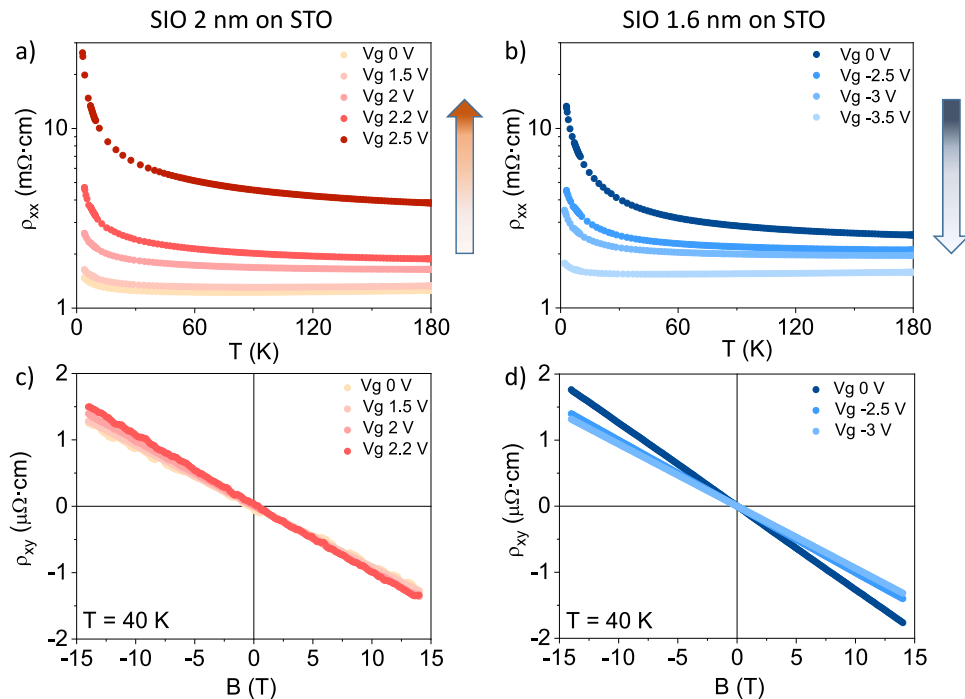


Fig. 3 Electrical measurements of 2 and 1.6 nm thickness SrIrO_3 samples for different gate voltages. Longitudinal resistivity (**a, b**) and Hall effect (**c, d**) were measured at 40 K at each gate voltage during ionic liquid gating experiments of a 2 nm SIO 113 sample at the metallic side of the MIT (**a, c**) and of a 1.6 nm sample at the insulating side (**b, d**).

the gating process. The strong suppression of the concentration of both carrier types indicates effects of the gating process beyond doping of a semimetal, which is expected to yield opposite changes of electrons and holes densities.

The gating process was checked to be reversible (though hysteretic), see Supplementary Section 1 and Supplementary Figure S1. This excludes doping by electric field generated oxygen vacancies, shown before to happen in the related SrRuO_3 compound³³. The reduction potential of Ir^{4+} is strongly negative and it has been observed that oxygen migration forced at high (reducing) voltages irreversibly damages SrSiO_3 turning it into an amorphous non stoichiometric Ir^{3+} oxide³⁴. The reversibility of the gating process support absence of oxygen vacancy generation. Moreover, oxygen outtake would degrade the double layer and modify its capacitance contrary to what it is observed (see Supplementary Fig. S2).

The anomalous reduction in both, electron and hole concentrations when the insulating state is approached, suggest the opening of a charge gap. However, the question remains why this phenomenon (if unrelated to doping) depends on the direction of the electric field. In principle, the applied electric field will change the strength of the confining potential and the magnitude of the spin-orbit interaction, but a dependence on the field direction, as experimentally observed, is not expected. As a result of the reduced carrier density, screening effects on the charge density are almost negligible, especially in the insulating state where the Thomas Fermi screening length becomes comparable to sample thickness. Therefore, the large partially screened electric field generated in the gating process can produce deep modifications of the electronic structure in a system, like ours, with broken symmetry and strong spin-orbit interaction. This indicates that symmetry breaking proper of ultrathin samples, possibly modulated by the electric field generated during the gating process, plays a leading role in the surprising asymmetric electric field dependence.

A direct indication of the correlated nature of the insulating state triggered by electric field is the unexpected (ferro)magnetism revealed by the low-temperature measurements of the transverse resistivity in the insulating state. Figure 4a–f show clear evidence of anomalous Hall effect in the insulating state between 2 and 40 K. Subtraction of the normal Hall resistivity obtained from the high field slope yields clear (inverted) hysteresis loops indicating that the anomalous Hall conductivity is negative (see Fig. 4g).

The insulator state has an out-of-plane remanence and is thus clearly different from other magnetic states found previously in perovskite iridates with in-plane moments such as the metamagnetic state found in SIO 214⁵ or the ferromagnetic state found in SIO 113/STO superlattices^{35–37}. Interestingly, the out-of-plane ferromagnetism is observed only in the insulating phase and was suppressed when the sample was brought to the metallic state.

Density functional theory calculations. The electric field modulation of the ground state of the SIO ultrathin films unearths an interesting scenario of external control of symmetry breaking. To gain insight in the electric field-driven modification of the SIO electronic states, we have performed first principles density functional theory (DFT) calculations. SIO films were modeled by asymmetric (001) SIO_m/STO slabs with two SrO layers at the free surface and at the SIO/STO interface. The supercells had four formula units in the plane to account for the reduction of the symmetry (observed in X-ray reciprocal space maps) due to anisotropic bond distortions produced by the rotation of oxygen octahedra and polar displacement of Sr atoms. See Supplementary Note 3 and Supplementary Figure S5. The number of unit cells (u.c.) in the (001) direction was varied between $m = 1$ and 6. The external electric field is added via a sawtoothlike potential, and conventional dipole corrections are used to avoid spurious electrostatic interactions between the periodically repeated

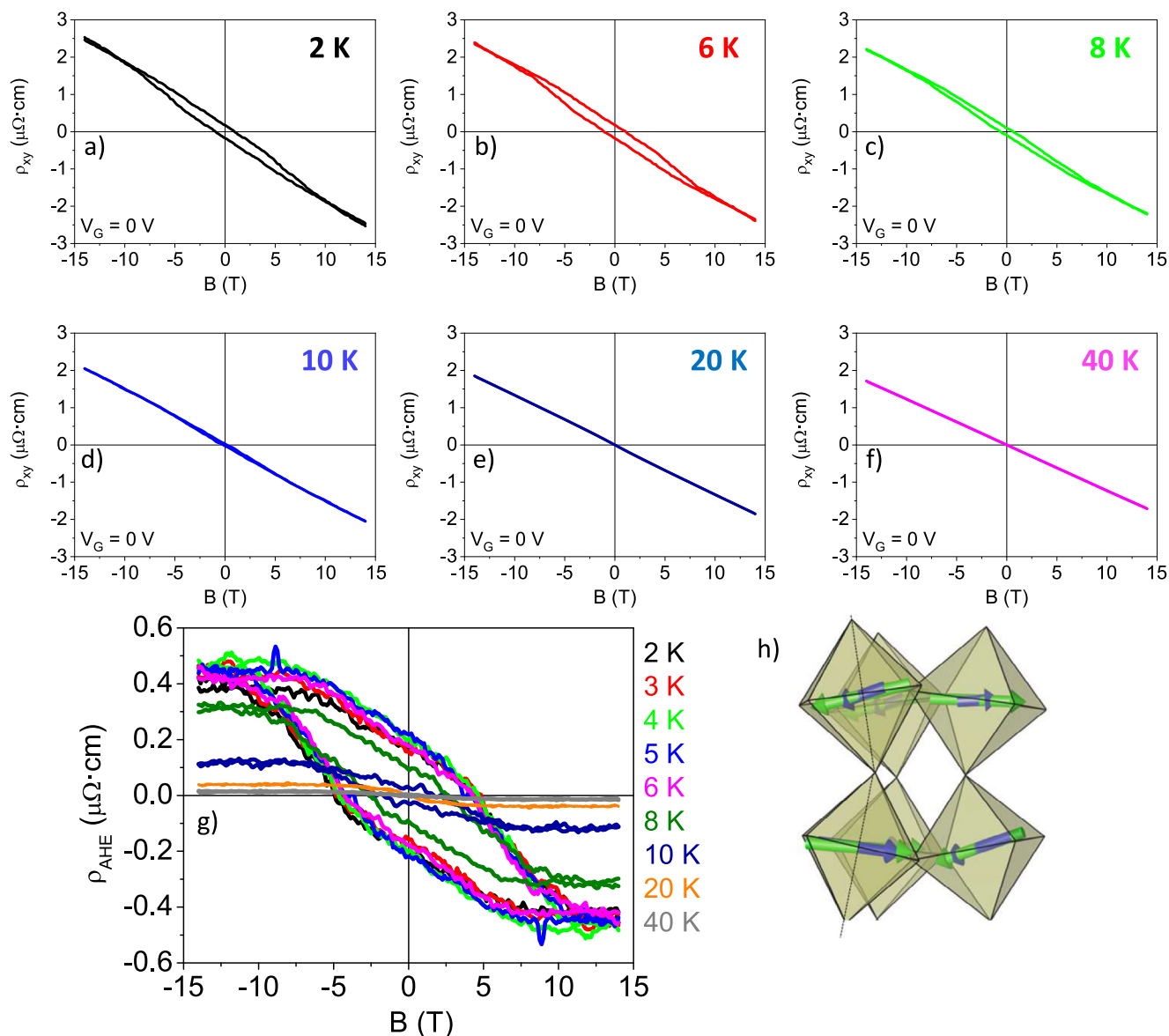


Fig. 4 Hall configuration measurements of the 1.6 nm thick SIO. **a–f** Hysteretic Anomalous Hall effect obtained measuring transverse resistivity as a function of magnetic field at low temperatures. **g** Anomalous Hall effect obtained subtracting the ordinary component to the transverse resistivity. **h** Sketch illustrating that the out of plane canted moment results from the bending of the Ir-O-Ir bonds or tilting of octahedra (Ir atoms are at the center and oxygen atoms are at the vertexes). Green and blue arrows represent orbital and spin moments as calculated by first principles (see below).

supercells³⁸. Structural optimization of the slab is then carried out to take into account the electrostatic screening effects.

For $m \leq 2$ the films are insulator and a MIT occurs for $m = 3$. In Fig. 5 the band structure around the Fermi level, E_F , of the SIO ($m = 3$)/STO slab is shown. The system is metallic, the band structure results from the cooperative interplay of electron hopping and spin-orbit interaction and is modulated by the tilting and rotation of the IrO_6 octahedra and the magnitude of the U Hubbard electron correlation. This band structure corresponds to the most stable $a^-a^-c^+$ crystal configuration observed in the x-ray analysis but with the rotation angles of the IrO_6 octahedra nearest to the SIO-STO interface modified by the proximity to the STO substrate. The plane-averaged Ir-O-Ir angle takes the values 176.0, 162.0, and 160.2 degrees with values decreasing from the interface to the surface. Besides hybridization with the oxygen p orbitals, substantial mixing of the $J_{\text{eff}} = 3/2$ and $J_{\text{eff}} = 1/2$ states is present in the occupied electronic bands, but the unoccupied electronic states have mainly $J_{\text{eff}} = 1/2$ character,

revealing that ultrathin SIO films are close to the $J_{\text{eff}} = 1/2$ single band limit. Different colors in the figure indicate projections into the individual IrO_2 planes in the structure (green corresponds to the surface, red to the middle, and blue to the immediate vicinity to the interface). Figure 5 also shows the corresponding band structures for the SIO/STO asymmetric slab under electric fields of $\pm 0.1 \text{ eV/\AA}$ perpendicular to the layers. A positive value corresponds to electric field pointing from the SIO surface to the interface with the STO and thus to positive gate voltages in the experiment.

It is found that the calculated ground state depends on the direction of the electric field. For positive electric fields, the width of the mixed orbital t_{2g} d band reduces significantly and the narrowed $J_{\text{eff}} = 1/2$ t_{2g} bands are pushed above the Fermi level yielding an insulating state. Conversely, wider bands cross the Fermi level for negative electric fields yielding a metallic state. Thus, there is an asymmetric effect of positive and negative electric fields on the width and energy position of the bands close

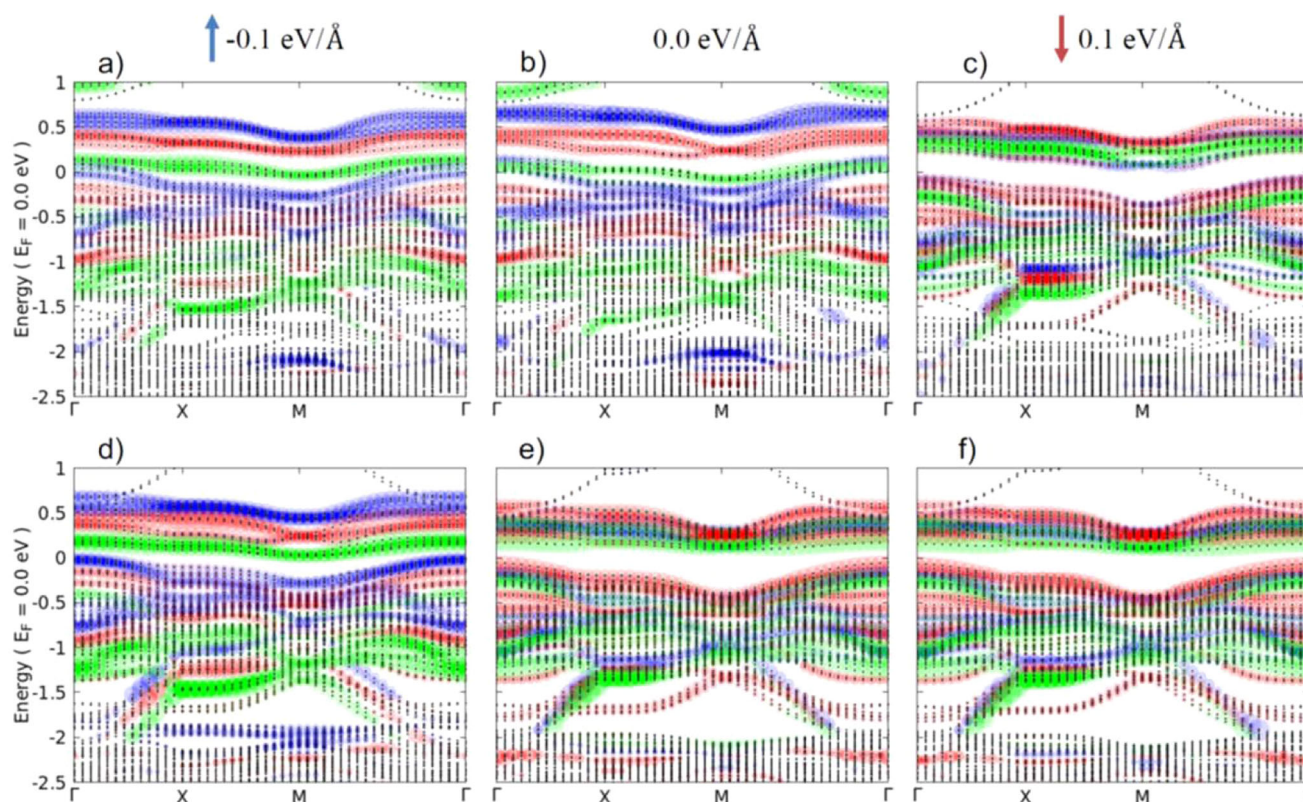


Fig. 5 Electronic structure from first principles simulations. Band dispersion for the SIO supercell on STO (**a–c**). Different colors correspond to projections of bands on the different IrO_2 planes in the structure (blue, red, and green correspond respectively to the first, second, and third closest IrO_2 plane to the STO interface). Calculations are under external electric fields $E = -0.1 \text{ eV/\AA}$ (**a**), $E = 0$ (**b**) and $E = +0.1 \text{ eV/\AA}$ (**c**). Band dispersion for the SIO supercell without the STO layer but without relaxing the atomic positions (**d–f**). Electric fields are $E = -0.1 \text{ eV/\AA}$ (**d**), $E = 0$ (**e**) and $E = +0.1 \text{ eV/\AA}$ (**f**).

to the Fermi energy. These calculations are in fact fully consistent with the experimental results described above. Notice that the electric field has a symmetry-breaking effect. Positive electric fields restore the degeneracy of the bands corresponding to the individual IrO_2 planes, already lifted in the asymmetric SIO/STO slab, and increase the energy of the bands mainly localized in IrO_2 planes at the film surface (green-colored bands in the figure), while for negative fields the bands remain non-degenerate. Therefore, electronic states corresponding to different planes appear separated in the metallic state, even at zero applied electric field, and mixed in the insulating state. Negative electric fields increase the film asymmetry while positive electric fields reduce it indicating the compensation of the intrinsic asymmetry of the film grown on STO.

It is important to note that the tuning of the metal-insulator transition by the positive electric field occurs only in the presence of the spin-orbit interaction. In calculations that do not include the spin-orbit interaction, the film is metallic and the electric field is screened by charge redistribution between the IrO_2 layers. (see Supplementary Figure S6).

The dependence of the electronic structure on the direction of the electric field indicates that the external electric field modulates a broken symmetry state of the structure. It may result from differences in the confining potentials of STO and vacuum at each side of the SIO slab or from structural asymmetries in the layer (see below). Direct evidence for this scenario is found from calculations (see bottom panels in Fig. 5) removing the STO layer while keeping the structure unrelaxed to maintain a certain degree of asymmetry. Notice that the removal of the STO (with the consequent reduction of band asymmetry) yields an insulating state at $E = 0$, and that a negative electric field does

not restore the metallic state, although reduces significantly the gap and increases the band asymmetry. This indicates that the inversion symmetry breaking introduced by the STO is similar to that of a negative electric field.

To further address the effect of the electric field in modulating the inversion asymmetry introduced by the STO substrate, we have examined the layer projected density of states for the three fields, $E = 0$ and $E = \pm 0.1 \text{ eV/\AA}$ in structures in which the STO substrate is present or removed from the supercell. Results are shown in Fig. 6. In the presence of the STO base layer, and in the absence of an external field, the SIO layers have a metallic density of states. Applying a positive field alters the energy distribution of the occupied bands, and there is a significant narrowing of the Ir d -bands particularly at the surface layer and the energy gap opens up. Conversely, the negative field causes a large rearrangement of the electronic levels within the film maintaining the density of states at the Fermi level. It is important to remark that, the number of electrons in each layer determined either from the integrated layer projected density of states or from the Bader charges (see Supplementary Note 3) is practically unaltered by the application of the electric field.

The second row of Fig. 6 displays the layer projected DOS of SIO slabs without the STO layer but with the atomic structure obtained in the calculation of the SIO/STO slabs (i.e. atomic relaxation is not performed). The insulating state is already found at $E = 0$ (instead of at the $E = +0.1 \text{ eV/\AA}$ found with STO) indicating that the effect of the intrinsic symmetry breaking is comparable to that of a negative electric field, i.e. pointing from STO to SIO surface. Relaxing the lattice positions in the symmetric SIO slab without STO produces an insulating state which, being the SIO slab now fully symmetric, is not modified

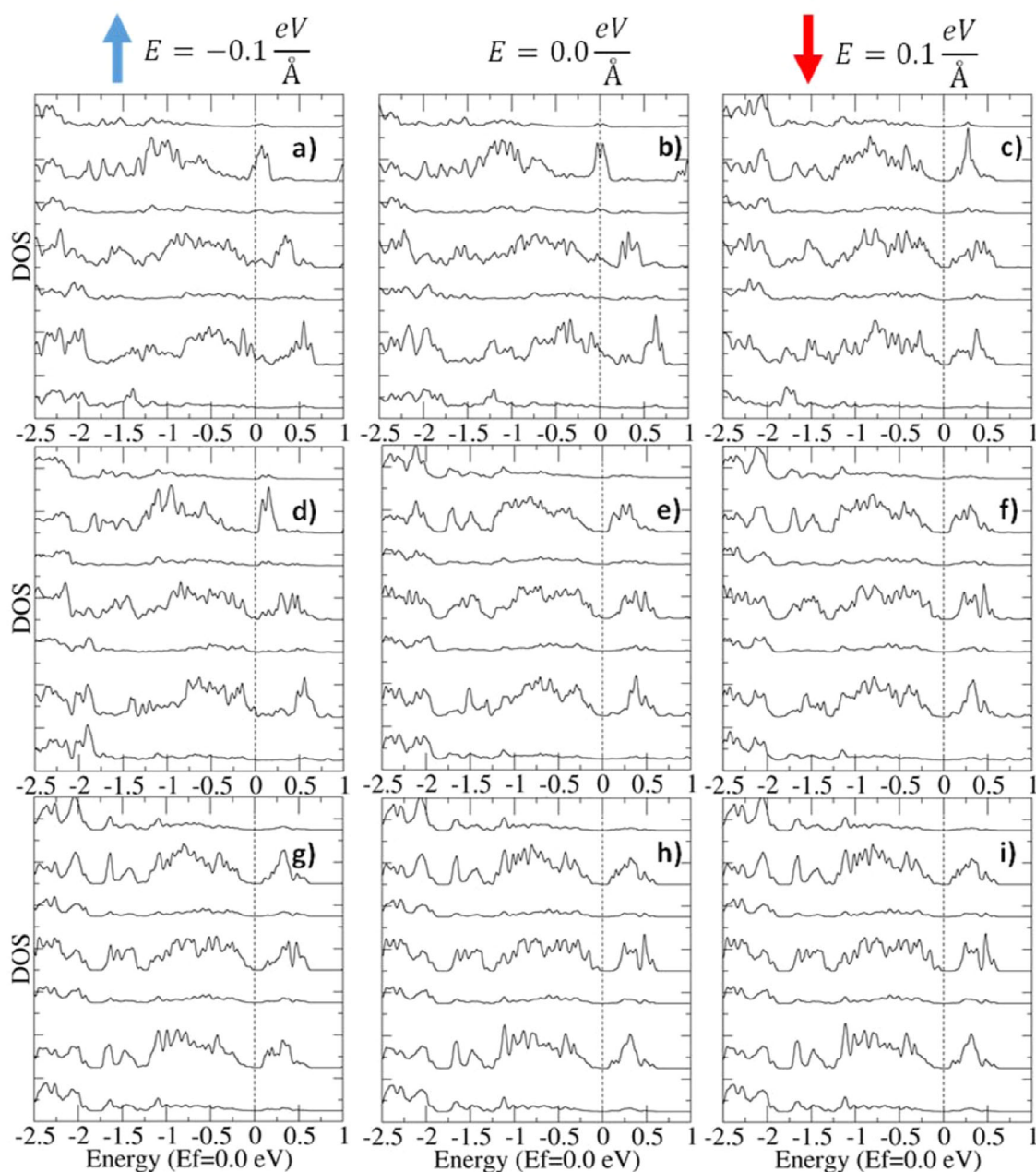


Fig. 6 Density of states projected to SIO (SrO, IrO₂,...) [001] lattice planes. The 3 columns correspond to the applied electric field with values $E = -0.1 \text{ eV/\AA}$ (a, d, g), $E = 0 \text{ eV/\AA}$ (b, e, h), and $E = +0.1 \text{ eV/\AA}$ (c, f, i) from left to right respectively. The three rows correspond to 3 SIO atomic models: SIO superstructure grown on STO (a–c), SIO superstructure without the STO layer but no relaxation of the atomic positions (d–f), and a fully symmetric structure without the STO layer and allowing relaxation of the atomic positions (g, h, j).

when the direction of the electric field is reversed. Data are shown in the three bottom panels of Fig. 6 for the same $E = 0$ and $E = \pm 0.1 \text{ eV/\AA}$ electric fields values. This result evidences that the cooperative effect of the electric field and the asymmetry of the slab induces the inversion symmetry breaking and triggers the metal-to-insulator transition in the system. An interesting result from the DFT calculations is the splitting of the bands corresponding to the individual IrO₂ planes of the slab, the bands mainly localized at the surface have always smaller energy. This indicates a larger spin orbit-driven symmetry-breaking effect of the applied electric field at the surface than at the interface and supplies an interesting clue for the understanding of the electric field-driven band splitting.

Discussion

A possible source of coupling of the electronic structure to the electric field is through the restoration of the orbital angular momentum degree of freedom in the t_{2g} manifold (effective $L = 1$). Orbital angular momentum couples to the inversion symmetry-breaking electric fields built up in ultrathin oxide layers, producing Rashba-type surface band splitting, which can be the source of exciting unexpected new effects in low dimensions driven by spin-orbit interaction and electron correlations³⁹. The coupling occurs through the interaction of the electric field with the dipolar charge distributions associated to orbital angular momentum states, and results in Rashba-type splitting^{40,41}. However, this would be at odds with the “up-down” electric field

asymmetry uncovered by the gating experiments and the first principles calculations.

Alternatively, the interplay between spin-orbit interaction and inversion symmetry breaking can be understood in terms of multi-orbital effects of Rashba spin-orbit interaction in t_{2g} electron^{17–20}. SIO is a t_{2g} electron system due to the splitting of d orbitals by the strong crystal field. While in a cubic environment the t_{2g} orbitals can be decoupled, as interorbital hopping is forbidden by parity symmetry, inversion symmetry breaking opens new hopping channels in the Ir-oxygen network, i.e. when an electron hops from a d_{zx} (d_{yz}) orbital to a neighboring O p_x (p_y) orbital in the y (x) direction, the matrix element is different from zero in the presence of a perpendicular electric field. Therefore, hopping processes will be modulated by the external electric field and when combined with the atomic-like spin-orbit interaction the new hopping channels give rise to additional Rashba band splittings, which in multi-orbital systems take a much complex form than the conventional spin-splitting in 2D semiconductor quantum wells¹⁷. The electric field itself breaks inversion symmetry, and it may thus modulate the effect of other forms of symmetry breaking in producing further polar deformations of the orbital lobes which ultimately open the new hopping channels. Although electric field only, does not distinguish up and down, the other forms of symmetry breaking may establish different amplitudes of the hopping integral at the surface and at the interface with the STO, which the electric field can modulate. In our case there is an asymmetry of the oxygen rotations at the interface (where the titanate suppresses the bending of out-of-plane bonds) as compared to the surface where the film relaxes towards the $a^-a^-c^+$ structure of the bulk). Octahedral rotations allow for antisymmetric inter orbital hopping terms between xy and yz orbitals along the x direction originating at the deformation of the orbital lobes of the surface layer¹⁸. Also, the missing apical oxygen above the surface lowers the energy of the z^2 orbital, allowing for new $t_{pd\pi}$ routes which have been proposed couple to the electric field¹⁷. Future work will be directed to establish the direct connection between the detailed mechanism and the broken symmetry of IrO₂ plane bands, but it is clear that the modulation of the broken symmetry hopping channels by the strong external electric field plays the central role in the observed effect and justifies the lower energy (larger hopping) of the IrO₂ planes at the surface.

Furthermore, and also in agreement with the experimental results, the calculated insulator phase for the SIO/STO under a positive electric field presents canted orbital (0.26 μ_B) and spin (0.17 μ_B) moments yielding out of plane components of 0.04 μ_B and 0.02 μ_B , respectively. Their ratio is 1.52, close to two, the ideal value of the $J_{\text{eff}} = 1/2$ state. Orbital and spin moments in neighboring Ir atoms align antiferromagnetically both in the same layer and between different layers, albeit, there is a canting of the magnetic moments associated with the rotation and tilting of the IrO₆ octahedra, yielding a weak ferromagnetic component perpendicular to the film, see Fig. 4h. On the contrary, in the metallic state reached by the application of the negative electric field, where, although smaller local orbital and spin moments may survive, the long-range magnetic order observed in the insulator does not occur. The small out of plane moments are produced by the canting of an antiferromagnetic state by the DMI⁴². The bending of out-of-plane Ir-O-Ir bonds establish, according to Bertaut rules⁴³, the symmetry conditions for the existence of the out-of-plane (weak) ferromagnetism⁴⁴. The anomalous Hall conductivity measured in the insulating phase reflects the canted antiferromagnetic order. The non-collinearity yielded by the strong spin-orbit interaction breaks time-reversal symmetry to meet the conditions to the observation of AHE^{45,46} which intrinsically originates at the Berry flux at avoided crossings prompted by symmetry breaking and spin-orbit interaction⁴⁷.

Conclusions

In summary, we have shown that in SrIrO₃ ultrathin films, the large electric fields generated in a field effect experiment with ionic liquids couple strongly to the electronic structure producing deep modifications, which are beyond those expected from doping. The electric field modulation of new inter-orbital hopping channels opened by the broken inversion symmetry explains the anomalous band splitting triggering the metal-to-insulator transition. The emergent anomalous Hall effect related to the out-of-plane canted antiferromagnetic state found in the insulating phase supplies solid evidence for the leading role played by electron correlations in yielding the transition. The picture emerges that the electric-field controlled inversion symmetry breaking provides an effective knob to modulate the effective strength of the correlations yielding the MIT transition.

A final remark concerns the finding of a canted antiferromagnetic insulating state tunable by an electric field. Ferromagnetic insulators are scarce, yet they are very useful in spintronics as spin filters or as electrodes in proximity interactions. On the other hand, metals with strong spin-orbit interaction are desirable as spin-charge converters. The possibility of switching between both with an electric field demonstrated in this work may inspire novel device concepts in low-dissipation oxide electronics⁴⁸.

Methods

Growth process. The 1–3 nm thick SIO thin films were grown on top of (001) oriented SrTiO₃ (STO) substrates by sputtering a stoichiometric target in high pressure (2.8 mbar) pure oxygen atmosphere and at a substrate temperature of 650 °C. Growth was followed by a 1-hour annealing at 650 °C in pure oxygen (1 atm). This technique produces highly perfect epitaxial layers of oxides at a slow rate (0.1 nm/min) which allows an accurate thickness control^{49,50}.

Fabrication and measurement of electric double-layer transistors. EDL transistors were fabricated 1–3 nm thick SIO thin films using the side gating geometry. Conventional optical lithography combined with reactive ion etching were used to define (250 micron) Hall bars with millimeter-size Au side gate contacts. This size of the Hall bars yielded in some occasions the anisotropic transport reported earlier due to coupling to STO structural domains⁵¹. The gate dielectric was formed by depositing a 1 μl drop of the ionic liquid DEME-TFSI. The DEME-TFSI was baked at 100 °C and at 10^{-2} Torr for a period of 24 hours. To avoid sample degradation by reaction with the ionic liquid it was deposited on the sample on a precooled cold plate inside a glove box filled with Ar gas. The gate voltage (V_G) was applied at 230 K for a period of 5 minutes and the device immediately cooled down to 10 K. Positive (negative) gate voltages correspond to electron (hole) doping. Magneto-transport characterization of the EDL transistors was conducted in a Quantum Design Physical Properties Measurement System (PPMS). Transport measurements (resistance and Hall effect) were recorded during the warming of the sample up to 180 K. For Hall measurements, magnetic fields were swept up to ± 14 T. To separate the Hall contribution, an antisymmetrization routine was conducted using:

$$\rho_{xy}^+(H) = \frac{\rho_{xy,RAW}^+(H) - \rho_{xy,RAW}^-(H)}{2}$$

$$\rho_{xy}^-(H) = \frac{\rho_{xy,RAW}^-(H) - \rho_{xy,RAW}^+(H)}{2}$$

where $\rho_{xy,RAW}^+(H)$ and $\rho_{xy,RAW}^-(H)$ are the positive and negative field sweep branches of the raw measurements of the transversal resistivity, which were been interpolating onto the same field. The effect of gating was reversible as far as samples were in the metallic state. Entering the insulating state resulted in hysteretical voltages to recover the metallic state, i.e., larger negative voltages than the positive ones required to drive the sample insulating. See Supplementary Figure S1. Reversible (though hysteretic) gating rules out doping by the migration of oxygen atoms in the SIO crystallographic unit cell^{52–54}. This was further confirmed by capacitance measurements of the double layer not showing changes due to electrochemical reactions at the liquid interfaces associated with the transport of oxygen ions. See Supplementary Figures S1 and S2.

X-ray diffraction reciprocal space maps. Reciprocal space maps were measured in a Bruker D8 Discover Microdiffractometer equipped with a two-dimensional Vantec detector, Hubber $\frac{1}{4}$ Eulerian cradle, video camera/laser alignment system,

and a Co K_{α} x-ray radiation point source ($\lambda = 1.79 \text{ \AA}$). The beam is conditioned with a graphite monochromator and the samples were mounted for reflection configuration. We used an 800 μm collimator and the sample-to-detector distance was kept at 20 cm. The diffractometer images acquired using the 2D detector were analyzed and combined to reconstruct the structure factor in 3D reciprocal space using a self-designed software tool (RS*App). A 3D view of the reciprocal space is obtained allowing the interpretation and analysis of the shape of the different poles of scattering as well as the projection of the data into different crystallographic axis and planes.

First-principles calculations. Ab-initio density functional theory (DFT) calculations have been performed using the projector augmented wave method employing the Vienna simulation package (VASP)^{55–57}. We adopted the generalized gradient approximation by Perdew-Burke-Ernzerhof (PBE) with a full treatment of relativistic effects (SOC) and including on-site Hubbard corrections in the form of the Dudarev approximation for a proper description of the electron correlation of the Ir 5d and Ti 3d orbitals. Values of 1.5 and 4.4 eV for the Ir and Ti d-bands effective Hubbard potential, respectively^{58,59} and a plane-wave energy cutoff of 500 eV have been used. We model the SIO films grown on STO by a (SIO)_m/STO supercell containing 4 in-plane SIO unit cells (u.c.) and *m* SIO and one STO u.c. along the out-of-plane direction, thus the slab contains $2 \times 2 \times (m + 1)$ pseudocubic u.c. The vacuum region included for detaching the supercell surfaces is 18 Å. In all the calculations, we took the lattice parameters of the STO after full relaxation. We allow for different configuration of the rotations and tilting of the IrO₆ octahedra network. We found that the ground state of the films is sensitive to the configuration of the rotation. For the calculations in presence of electric field, a sawtooth-like potential is applied and dipolar corrections are included. The atomic relaxations of the slab are carried out in absence and presence of the electric field until the Hellman-Feynman forces on each atom becomes <0.015 eV/Å. The structural optimization of the slab with the field is important to take into account the electrostatic screening effects. In presence of the electric field no significant ferroelectric-like ionic displacements, were obtained.

Data availability

The data used in this paper are available from the authors upon reasonable request

Received: 16 December 2022; Accepted: 7 May 2023;

Published online: 24 May 2023

References

- Witczak-Krempa, W., Chen, G., Kim, Y. B. & Balents, L. Correlated quantum phenomena in the strong spin-orbit regime. *Annu. Rev. Condens. Matter Phys.* **5**, 57–82 (2014).
- Watanabe, H., Shirakawa, T. & Yunoki, S. Microscopic study of a spin-orbit-induced Mott insulator in Ir oxides. *Phys. Rev. Lett.* **105**, 19–22 (2010).
- Cao, G., Bolivar, J., McCall, S., Crow, J. & Guertin, R. Weak ferromagnetism, metal-to-nonmetal transition, and negative differential resistivity in single-crystal. *Phys. Rev. B* **57**, R11039–R11042 (1998).
- Kim, B. J. et al. unprecedented $jeff = 1/2$ mott state induced by relativistic spin-orbit coupling in Sr₂IrO₄. *Phys. Rev. Lett.* **101**, 1–4 (2008).
- Kim, B. J. et al. Phase-sensitive observation of a spin-orbital mott state in Sr₂IrO₄. *Science* **323**, 1329–1332 (2009).
- Moon, S. J. et al. Dimensionality-controlled insulator-metal transition and correlated metallic state in 5d transition metal oxides Sr_{n+1}Ir_nO_{3n+1} (*n*=1, 2, and ∞). *Phys. Rev. Lett.* **101**, 2–5 (2008).
- Yamasaki, A. et al. Three-dimensional electronic structures and the metal-insulator transition in Ruddlesden-Popper iridates. *Phys. Rev. B* **94**, 1–10 (2016).
- Zhang, H., Haule, K. & Vanderbilt, D. Effective $J=1/2$ insulating state in Ruddlesden-Popper iridates: an LDA+DMFT study. *Phys. Rev. Lett.* **111**, 1–5 (2013).
- Kawasaki, J. K., Uchida, M., Paik, H., Schlom, D. G. & Shen, K. M. Evolution of electronic correlations across the rutile, perovskite, and Ruddlesden-Popper iridates with octahedral connectivity. *Phys. Rev. B* **94**, 1–6 (2016).
- Kawasaki, J. K. et al. Rutile IrO₂/TiO₂ superlattices: a hyperconnected analog to the Ruddlesden-Popper structure. *Phys. Rev. Mater.* **2**, 1–7 (2018).
- Nie, Y. F. et al. Interplay of spin-orbit interactions, dimensionality, and octahedral rotations in semimetallic SrIrO₃. *Phys. Rev. Lett.* **114**, 1–6 (2015).
- Groenendijk, D. J. et al. Spin-orbit semimetal SrIrO₃ in the two-dimensional limit. *Phys. Rev. Lett.* **119**, 2–7 (2017).
- Schütz, P. et al. Dimensionality-driven metal-insulator transition in spin-orbit-coupled SrIrO₃. *Phys. Rev. Lett.* **119**, 1–6 (2017).
- Dresselhaus, G. Spin-orbit coupling effects in zinc blende structures*. *Phys. Rev.* **100**, 580 (1954).
- Rashba, E. I. Properties of semiconductors with an extremum loop. Cyclotron and combinational resonance in a magnetic field perpendicular to the plane of the loop. *Sov. Phys. Solid State* **2**, 1109–1122 (1960).
- Bychkov, Y. A. & Rashba, E. I. Properties of a 2D electron gas with lifted spectral degeneracy. *JETP Lett.* **39**, 78–81 (1984).
- Khalsa, G., Lee, B. & Macdonald, A. H. Theory of t_{2g} electron-gas Rashba interactions. *Phys. Rev. B* **88**, 1–5 (2013).
- Zhong, Z., Tóth, A. & Held, K. Theory of spin-orbit coupling at LaAlO₃/SrTiO₃ interfaces and SrTiO₃ surfaces. *Phys. Rev. B* **87**, 1–5 (2013).
- Kim, Y., Lutchyn, R. M. & Nayak, C. Origin and transport signatures of spin-orbit interactions in one- and two-dimensional SrTiO₃-based heterostructures. *Phys. Rev. B* **87**, 1–11 (2013).
- Shanavas, K. V., Popović, Z. S. & Satpathy, S. Theoretical model for Rashba spin-orbit interaction in d electrons. *Phys. Rev. B* **90**, 1–9 (2014).
- Shimotani, H. et al. Insulator-to-metal transition in ZnO by electric double layer gating. *Appl. Phys. Lett.* **91**, 10–13 (2007).
- Ueno, K. et al. Electric-field-induced superconductivity in an insulator. *Nat. Mater.* **7**, 855–858 (2008).
- Yuan, H. et al. High-density carrier accumulation in ZnO field-effect transistors gated by electric double layers of ionic liquids. *Adv. Funct. Mater.* **19**, 1046–1053 (2009).
- Ye, J. T. et al. Liquid-gated interface superconductivity on an atomically flat film. *Nat. Mater.* **9**, 125–128 (2010).
- Yamada, Y. et al. Electrically induced ferromagnetism at room temperature in cobalt-doped titanium dioxide. *Science* **332**, 1065–1067 (2011).
- Leng, X., Garcia-Barriocanal, J., Bose, S., Lee, Y. & Goldman, A. M. Electrostatic control of the evolution from a superconducting phase to an insulating phase in ultrathin YBa₂Cu₃O_{7-x} films. *Phys. Rev. Lett.* **107**, 6–9 (2011).
- Bollinger, A. T. et al. Superconductor-insulator transition in La_{2-x}Sr_xCuO₄ at the pair quantum resistance. *Nature* **472**, 458–460 (2011).
- Ohuchi, Y. et al. Electric-field control of anomalous and topological Hall effects in oxide bilayer thin films. *Nat. Commun.* **9**, 1–7 (2018).
- Glazer, A. M. Simple ways of determining perovskite structures. *Acta Crystallogr. Sect. A* **31**, 756–762 (1975).
- Choquette, A. K. et al. Octahedral rotation patterns in strained EuFeO₃ and other Pbnm perovskite films: Implications for hybrid improper ferroelectricity. *Phys. Rev. B* **94**, 1–8 (2016).
- Liu, J. et al. Tuning the electronic properties of $J_{\text{eff}}=1/2$ correlated semimetal in epitaxial perovskite SrIrO₃. 1–5 (2013).
- Manca, N. et al. Balanced electron-hole transport in spin-orbit semimetal SrIrO₃ heterostructures. *Phys. Rev. B* **97**, 2–6 (2018).
- Yi, H. T. et al. Tuning the metal-insulator crossover and magnetism in SrRuO₃ by ionic gating. *Sci. Rep.* **4**, 6604 (2014).
- Wan, G. et al. Amorphization mechanism of SrIrO₃ electrocatalyst: how oxygen redox initiates ionic diffusion and structural reorganization. *Sci. Adv.* **7**, eabc7323 (2021).
- Matsuno, J. et al. Engineering a spin-orbital magnetic insulator by tailoring superlattices. *Phys. Rev. Lett.* **114**, 1–5 (2015).
- Hao, L. et al. Two-dimensional $Je_{\text{ff}} = 1/2$ antiferromagnetic insulator unraveled from interlayer exchange coupling in artificial perovskite iridate superlattices. *Phys. Rev. Lett.* **119**, 1–6 (2017).
- Hao, L. et al. Giant magnetic response of a two-dimensional antiferromagnet. *Nat. Phys.* **14**, 806–810 (2018).
- Meyer, B. & Vanderbilt, D. Ab initio study of BaTiO₃ and PbTiO₃ surfaces in external electric fields. *Phys. Rev. B* **63**, 1–10 (2001).
- Sunko, V. et al. Maximal Rashba-like spin splitting via kinetic-energy-coupled inversion-symmetry breaking. *Nature* **549**, 492–496 (2017).
- Park, S. R., Kim, C. H., Yu, J., Han, J. H. & Kim, C. Orbital-angular-momentum based origin of rashba-type surface band splitting. *Phys. Rev. Lett.* **107**, 1–5 (2011).
- Oh, S. & Choi, H. J. Orbital angular momentum analysis for giant spin splitting in solids and nanostructures. *Sci. Rep.* **7**, 1–10 (2017).
- Khomskii, D. I. Transition metal compounds. (Cambridge University Press, 2014). <https://doi.org/10.1017/CBO9781139096782>.
- Bertaut, E. F. Magnetism. in (eds. Rado, G. T. & Suhl, H.) 149 (New York: Academic Press, 1965).
- Bousquet, E. & Cano, A. Non-collinear magnetism in multiferroic perovskites. *J. Phys. Condens. Matter* **28**, 123001 (2016).
- Chen, H., Niu, Q. & Macdonald, A. H. Anomalous hall effect arising from noncollinear antiferromagnetism. *Phys. Rev. Lett.* **112**, 1–5 (2014).
- Nakatsui, S., Kiyohara, N. & Higo, T. Large anomalous Hall effect in a non-collinear antiferromagnet at room temperature. *Nature* **527**, 212–215 (2015).
- Šmejkal, L., Mokrousov, Y., Yan, B. & MacDonald, A. H. Topological antiferromagnetic spintronics. *Nat. Phys.* **14**, 242–251 (2018).
- Manipatruni, S. et al. Scalable energy-efficient magnetoelectric spin-orbit logic. *Nature* **565**, 35–42 (2019).
- Varela, M. et al. Intracell changes in epitaxially strained YBa₂Cu₃O_{7-x} ultrathin layers in YBa₂Cu₃O_{7-x}/PrBa₂Cu₃O₇ superlattices. *Phys. Rev. Lett.* **83**, 3936–3939 (1999).

50. Varela, M. et al. Direct evidence for block-by-block growth in high-temperature superconductor ultrathin films. *Phys. Rev. Lett.* **86**, 5156–5159 (2001).
51. Van Thiel, T. C. et al. Coupling lattice instabilities across the interface in ultrathin oxide heterostructures. *ACS Mater. Lett.* **2**, 389–394 (2020).
52. Jeong, J. et al. Suppression of metal-insulator transition in VO₂ by electric field-induced oxygen vacancy formation. *Science* **339**, 1402–1405 (2013).
53. Li, M. et al. Suppression of ionic liquid gate-induced metallization of SrTiO₃(001) by oxygen. *Nano Lett.* **13**, 4675–4678 (2013).
54. Perez-Muñoz, A. M. et al. In operando evidence of deoxygenation in ionic liquid gating of YBa₂Cu₃O_{7-x}. *Proc. Natl. Acad. Sci. USA.* **114**, 215–220 (2017).
55. Kresse, G. & Furthmüller, J. Efficient iterative schemes for ab initio total-energy calculations using a plane-wave basis set. *Phys. Rev. B* **54**, 11169–11186 (1996).
56. Kresse, G. & Joubert, D. From ultrasoft pseudopotentials to the projector augmented-wave method. *Phys. Rev. B* **59**, 1758–1775 (1999).
57. Kresse, G. & Hafner, J. Ab initio molecular dynamics for liquid metals. *Phys. Rev. B* **47**, 558–561 (1993).
58. Okamoto, S., Millis, A. J. & Spaldin, N. A. Lattice relaxation in oxide heterostructures: LaTiO₃/SrTiO₃ superlattices. *Phys. Rev. Lett.* **97**, 4–7 (2006).
59. Kim, B., Liu, P. & Franchini, C. Dimensionality-strain phase diagram of strontium iridates. *Phys. Rev. B* **95**, 1–7 (2017).

Acknowledgements

The authors acknowledge receiving funding from the project To2Dox of FlagERA ERA-NET Cofund implemented within the European Union's Horizon Europe Program. Work (J.S., C.L., F.M., M.G.-H.) supported by Spanish AEI through grants, PID2020-118078RB-I00 and by Regional Government of Madrid CAM through SINERGICO project Y2020/NMT-6661 CAIRO-CM. G.S.-S. acknowledges financial support from Spanish MCI Grant Nos. RTI2018-099054-J-I00 (MCI/AEI/FEDER, UE) and IJC2018-038164-I. M.C.M. acknowledges the financial support provided by PID2021-122980OB-C55. J.I.B. acknowledges the financial support provided by PID2021-122980OB-C51 and computational support provided by the Red Española de Supercomputación under the projects FI-2018-1-0038 and FI-2019-3-0034.

Author contributions

F.G., J.T., A.P. prepared the samples and did the electric field experiments with the help of F.J.M., C.M., and M.G.H. J.G.B., G.Y., G.R. did the x ray polar figures. M.C. and G.S.S. did electron microscopy characterization. Z.S. did the magnetic characterization.

F.G. and A.R.C. did the capacitance experiments. F.G., D.S.M., and F.C. did the fitting of the data to the 2-band model. J.I.B. and M.C.M. did the theory analysis. M.C.M., C.L., and J.S. wrote the manuscript with input and help of all authors.

Competing interests

The authors declare no competing interests.

Additional information

Supplementary information The online version contains supplementary material available at <https://doi.org/10.1038/s43246-023-00362-7>.

Correspondence and requests for materials should be addressed to Jacobo Santamaria.

Peer review information *Communications Materials* thanks the anonymous reviewers for their contribution to the peer review of this work. Primary Handling Editor: Aldo Isidori.

Reprints and permission information is available at <http://www.nature.com/reprints>

Publisher's note Springer Nature remains neutral with regard to jurisdictional claims in published maps and institutional affiliations.



Open Access This article is licensed under a Creative Commons Attribution 4.0 International License, which permits use, sharing, adaptation, distribution and reproduction in any medium or format, as long as you give appropriate credit to the original author(s) and the source, provide a link to the Creative Commons license, and indicate if changes were made. The images or other third party material in this article are included in the article's Creative Commons license, unless indicated otherwise in a credit line to the material. If material is not included in the article's Creative Commons license and your intended use is not permitted by statutory regulation or exceeds the permitted use, you will need to obtain permission directly from the copyright holder. To view a copy of this license, visit <http://creativecommons.org/licenses/by/4.0/>.

© The Author(s) 2023